Rough layer scattering filled by elliptical cylinders from the method of moments combined with the characteristic basis function method and the Kirchoff approximation

Christophe Bourlier

Research Article | Vol. 38, No. 9 / September 2021 / Journal of the Optical Society of America A | 1

Journal of the Optical Society of America A
OPTICS, IMAGE SCIENCE, AND VISION

Rough layer scattering filled by elliptical cylinders from the method of moments combined with the characteristic basis function method and the Kirchoff approximation

Christophe Bourlier

IETR (Institut d'Electronique et des Technologies du numéRique) Laboratory, UMR CNRS 6164, University of Nantes, La Chantrerie, Nantes, France (christophe.bourlier@univ-nantes.fr)

Received 28 April 2021; revised 19 August 2021; accepted 27 August 2021; posted 30 August 2021 (Doc. ID 430309); published 0 MONTH 0000

In this paper, the electromagnetic field scattered by several 2D scatterers of any shape is calculated rigorously from the boundary integral equations discretized by the method of moments with the point matching method and pulse basis functions. In addition, the resulting linear system is efficiently solved from the domain decomposition method named the characteristic basis function method. To accelerate the computation of the primary basis functions, which requires solving sublinear systems, the Kirchoff approximation is applied for metallic and dielectric objects. The efficiency of the method is tested on several applications met in practice: stack of rough interfaces separating homogeneous media, collection of metallic and dielectric elliptical cylinders, collection of coated elliptical cylinders, and a combination of the previous scenarios.

https://doi.org/10.1364/JOSAA.430309

1. INTRODUCTION

The study of the wave scattering from several scatterers of any shape is a subject of great interest. The applications of such research concern many areas such as remote sensing, radar surveillance, optics, and ocean acoustics.

For a collection of objects of canonical shape, like circular cylinders (of infinite length) and spheres, the scattered field can be computed analytically by introducing special functions, e.g., Bessel's and spherical Bessel's [1,2]. For elliptical cylinders [3–5], Mathieu's functions [6] are introduced, but they are difficult to program, unlike well-known Bessel's functions. Adding a boundary, like a smooth plate of infinite area (space divided into two media), the previous formulations can be extended [7–17], and the difficulty of programming increases. For a stack of rough interfaces separating homogeneous media, asymptotic approaches, in which simplifying assumptions are introduced, have been developed. For small roughness, we can cite the small perturbation method [18–24] and, for high roughness, the geometric optics approximation [25–27]. For a complex scenario, like inhomogeneous (dielectric objects are present in the layer) layered rough interfaces, it is difficult to derive a closed-form expression of the scattered field.

The well-known method of moments (MoM) [28–31] is a way of rigorously solving this type of scattering problem by converting the boundary integral equations into a linear system, in which the impedance matrix must be inverted to determine the surface currents. However, the direct solution of the linear system through a direct lower upper (LU) decomposition is usually limited by $\mathcal{O}(N^3)$ and $\mathcal{O}(N^2)$ complexities in CPU time and memory requirements, respectively, where N is the number of unknowns. This is computationally expensive for an electrically large multiscale object or a collection of dielectric objects (i.e., many unknowns) and has led to develop iterative methods and/or domain decomposition methods that significantly reduce the storage and computation cost. Among the numerous publications addressing this issue, references [32–43] have shown the efficiency of these methods for the scattering from a stack of two or three rough interfaces and for an object near a rough interface.

The characteristic basis function method (CBFM), a domain decomposition method, has shown efficiency for scattering from a 3D metallic or dielectric object [40,43–45]. In this paper, this method is applied for the scattering from P 2D metallic and dielectric scatterers of any shape. The propagation inside layer expansion (PILE) method [46] and its updated versions [39,42] can be extended for this type of problem; however, the difficulty of programming significantly increases. Thus, this method is not chosen. In addition, the subdomain decomposition iterative method (SDIM) [45,47] applied on the scenarios presented in this paper does not converge.

The CBFM principle splits up the problem into subproblems of smaller size, each of them being solved separately by

calculating the primary basis functions (PBFs). Next, the coupling between them is accounted for via the computation of the characteristic matrix, which involves the coupling matrices between the subproblems. To accelerate the calculation of PBFs, which requires one to solve sublinear systems, the Kirchoff approximation (KA) is applied for metallic and dielectric objects. The efficiency of the method is tested on several applications met in practice: stack of rough interfaces separating homogeneous media, collection of metallic and dielectric elliptical cylinders, collection of coated elliptical cylinders, and a combination of the previous scenarios.

The paper is organized as follows. Section 2 extends the MoM to P scatterers of any shape. Section 3 briefly summarizes the CBFM. Section 4 addresses the KA approximation for the derivation of the PBFs. Section 5 presents numerical results on four scenarios. The last section gives concluding remarks.

2. METHOD OF MOMENTS FOR SEVERAL SCATTERERS

This section presents the MoM for solving the electromagnetic wave scattering from several scatterers. For one and two scatterers, this approach is thoroughly explained in the textbook [30]. To sum, the boundary integral equations are applied on each scatterer and are discretized from the MoM by using the point-matching method and the pulse basis function. This leads to the linear system $\bar{\boldsymbol{Z}}\boldsymbol{X} = \boldsymbol{b}$, in which $\bar{\boldsymbol{Z}}$ is the impedance matrix of the two scatterers, $\boldsymbol{b}$ is a vector related to the incident field on the scatterers, and $\boldsymbol{X}$ the surface currents on the scatterers, i.e., the unknowns of the problem. In this section, this approach is generalized to several scatterers.

A. Case of a Single Illuminated Scatterer

For a single scatterer as shown in Fig. 1, the impedance matrix is expressed from four submatrices as

$$\bar{\boldsymbol{Z}}_{11} = \begin{bmatrix} \bar{\boldsymbol{A}}_{11} & \bar{\boldsymbol{B}}_{11} \\ \bar{\boldsymbol{C}}_{11} & \bar{\boldsymbol{D}}_{11} \end{bmatrix}. \tag{1}$$

The matrix $\bar{\boldsymbol{A}}_{11}$ is the matrix obtained from the Neumann boundary condition, i.e., when the scatterer is assumed to be perfectly conducting (metallic), and the transverse electric (TE) polarization is considered. It is calculated in the incident medium Ω_0. The matrix $\bar{\boldsymbol{B}}_{11}$ is the matrix obtained from the Dirichlet boundary condition, i.e., when the scatterer is assumed to be perfectly conducting (metallic), and the transverse magnetic (TM) polarization is considered. It is calculated in the incident medium Ω_0. The matrices $\{\bar{\boldsymbol{C}}_{11}, \bar{\boldsymbol{D}}_{11}\}$ are similar to the matrices $\{\bar{\boldsymbol{A}}_{11}, \bar{\boldsymbol{B}}_{11}\}$, but they are computed in the medium Ω_1. The elements of these four submatrices are given in Appendix A.

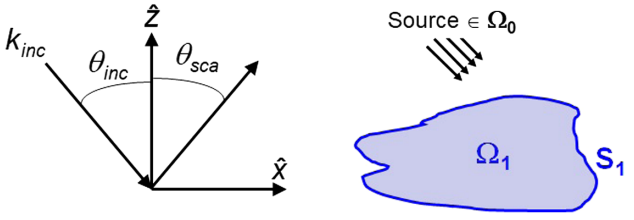

Fig. 1. Scattering from a single scatterer.

The vector $\boldsymbol{b}_1$ is defined as

$$\boldsymbol{b}_1 = \begin{bmatrix} \boldsymbol{b}_1' \\ \boldsymbol{0} \end{bmatrix} = \Big[\underbrace{\psi_{\text{inc}}(\boldsymbol{r}_1) \ldots \psi_{\text{inc}}(\boldsymbol{r}_{N_1})}_{\boldsymbol{b}_1^{\mathrm{T}},\, \boldsymbol{r}\in S_1} \underbrace{0 \ldots 0}_{N_1 \text{ times}} \Big]^{\mathrm{T}}, \tag{2}$$

where ψ_{inc} is the incident wave illuminating the scatterer. The symbol T stands for the transpose operator, and N_1 is the number of discretization points on the surface S_1 of the object. This means that the size of the matrix is $2N_1 \times 2N_1$.

The unknown vector $\boldsymbol{X}_1$ of length $2N_1$ is expressed as

$$\boldsymbol{X}_1 = \Big[\psi_1(\boldsymbol{r}_1) \ldots \psi_1(\boldsymbol{r}_{N_1}) \ \tfrac{\partial\psi_1(\boldsymbol{r}_1)}{\partial n} \ldots \tfrac{\partial\psi_1(\boldsymbol{r}_{N_1})}{\partial n} \Big]^{\mathrm{T}} \quad \boldsymbol{r}_{p\in[1;N_1]} \in S_1, \tag{3}$$

where $\partial\psi_1/\partial n = \nabla\psi_1 \cdot \hat{\boldsymbol{n}}_1$ is the normal derivative, in which $\hat{\boldsymbol{n}}_1$ is the unitary vector normal to S_1. The unknown $\boldsymbol{X}_1$ on S_1 is computed from $\boldsymbol{X}_1 = \bar{\boldsymbol{Z}}_{11}^{-1}\boldsymbol{b}_1$. The scattered field $\bar{\boldsymbol{\psi}}_{\text{sca}}(\boldsymbol{r})$ in the medium $\boldsymbol{r} \in \Omega_0$ is then obtained from the Huygens principle expressed as

$$\bar{\boldsymbol{\psi}}_{\text{sca}}(\boldsymbol{r}) = -\bar{\boldsymbol{P}}(\boldsymbol{r}, \boldsymbol{r}_1)\boldsymbol{X}_1, \tag{4}$$

where

$$\bar{\boldsymbol{P}}(\boldsymbol{r}, \boldsymbol{r}_1) = \begin{bmatrix} \bar{\boldsymbol{A}}_{ij} \\ \bar{\boldsymbol{B}}_{ij} \end{bmatrix}_{\boldsymbol{r}_j=\boldsymbol{r}_1, \boldsymbol{r}_i=\boldsymbol{r}}, \tag{5}$$

and $\boldsymbol{r}_1 \in S_1$ $(\boldsymbol{r} \neq \boldsymbol{r}_1)$. If $\boldsymbol{r} \in \Omega_1$ $(\boldsymbol{r} \neq \boldsymbol{r}_1)$; then, Eq. (4) is applied by taking the plus sign (instead of minus). The matrices $\{\bar{\boldsymbol{A}}_{ij}, \bar{\boldsymbol{B}}_{ij}\}$ are expressed in Appendix A.

The matrix $\bar{\boldsymbol{P}}(\boldsymbol{r}, \boldsymbol{r}_1)$ propagates the surface currents $\{\psi_1, \partial\psi_1/\partial n\}$ from $\boldsymbol{r}_1$ to $\boldsymbol{r}$. Its size is $N_{\text{sca}} \times (2N_1)$, where N_{sca} is the number of observation points and $\bar{\boldsymbol{\psi}}_{\text{sca}}$ is a vector of length N_{sca}.

In the far field ($kr \gg 1$, where k is the wavenumber of the medium), the propagation matrix can be simplified as [30]

$$\bar{\boldsymbol{P}}^{\infty}(\boldsymbol{r}, \boldsymbol{r}_1) = \frac{j}{4}\sqrt{\frac{2}{\pi kr}}\, e^{-j(\pi/4+kr)} \begin{bmatrix} j v_1 \boldsymbol{k}_{\text{sca}} \cdot \hat{\boldsymbol{n}}_1 e^{-j\boldsymbol{k}_{\text{sca}}\cdot\boldsymbol{r}_1}\sqrt{1+\gamma_1^2}\Delta_1 \\ e^{-j\boldsymbol{k}_{\text{sca}}\cdot\boldsymbol{r}_1}\sqrt{1+\gamma_1^2}\Delta_1 \end{bmatrix}, \tag{6}$$

where $\boldsymbol{k}_{\text{sca}} = k(\hat{\boldsymbol{x}}\sin\theta_{\text{sca}} + \hat{\boldsymbol{z}}\cos\theta_{\text{sca}})$ (see Fig. 1) stands for the direction of observation, γ_1 the slope of S_1 at the point $\boldsymbol{r}_1$, Δ_1 its sampling step, and $v_1 = \text{sgn}(\hat{\boldsymbol{n}}_1 \cdot \hat{\boldsymbol{z}})$ (sgn stands for the sign function).

The radar cross section (RCS) is written as [30]

$$\bar{\text{RCS}} = \lim_{r\to\infty} 2\pi r \left|\bar{\boldsymbol{\psi}}_{\text{sca}}(\boldsymbol{r})\right|^2 = \frac{1}{4k}\left| \begin{bmatrix} j v_1 \boldsymbol{k}_{\text{sca}} \cdot \hat{\boldsymbol{n}}_1 e^{-j\boldsymbol{k}_{\text{sca}}\cdot\boldsymbol{r}_1}\sqrt{1+\gamma_1^2}\Delta_1 \\ e^{-j\boldsymbol{k}_{\text{sca}}\cdot\boldsymbol{r}_1}\sqrt{1+\gamma_1^2}\Delta_1 \end{bmatrix} \boldsymbol{X}_1 \right|^2, \tag{7}$$

where $\bar{\text{RCS}}$ is a vector of the same length as $\bar{\boldsymbol{\psi}}_{\text{sca}}(\boldsymbol{r})$.

The normalized radar cross section (NRCS, dimensionless) is written as [29,30]

$$\mathbf{NRCS} = \lim_{r\to\infty} \frac{r}{2\eta_0} \frac{|\bar{\boldsymbol{\psi}}_{\text{sca}}(\boldsymbol{r})|^2}{p_{\text{inc}}}, \tag{8}$$

where η_0 is the wave impedance of medium Ω_0 and p_{inc} the incident power. For an incident plane wave of unitary amplitude, $p_{\text{inc}} = L\cos\theta_{\text{inc}}/(2\eta_0)$, so that $\mathbf{NRCS} = \mathbf{RCS}\cos\theta_{\text{inc}}/(2\pi L)$.

B. Case of *P* Illuminated Scatterers

For the case of two illuminated scatterers (Fig. 2, with $P = 2$), the impedance matrix $\bar{\boldsymbol{Z}}$ is expressed as [30]

$$\bar{\boldsymbol{Z}} = \begin{bmatrix} \bar{\boldsymbol{Z}}_{11} & \bar{\boldsymbol{Z}}_{12}^{(1)} \\ \bar{\boldsymbol{Z}}_{21}^{(1)} & \bar{\boldsymbol{Z}}_{22} \end{bmatrix}, \tag{9}$$

where $\bar{\boldsymbol{Z}}_{11}$ [Eq. (1)] and $\bar{\boldsymbol{Z}}_{22}$ are the self-impedance matrices of scatterers 1 and 2, respectively. The matrix $\bar{\boldsymbol{Z}}_{22}$ is obtained from $\bar{\boldsymbol{Z}}_{11}$ by changing (S_1, k_1) to (S_2, k_2), where $k_i = k_0\sqrt{\epsilon_{r,i}}$ is the wavenumber of the medium Ω_i of relative permittivity $\epsilon_{r,i}$. In addition, $k_0 = 2\pi/\lambda_0$ is the wavenumber in vacuum and λ_0 the wavelength in vacuum.

The coupling (interaction between two different scatterers) matrices $\bar{\boldsymbol{Z}}_{12}^{(1)}$ (of size $2N_1 \times 2N_2$) and $\bar{\boldsymbol{Z}}_{21}^{(1)}$ (of size $2N_2 \times 2N_1$) are written as

$$\bar{\boldsymbol{Z}}_{12}^{(1)} = \begin{bmatrix} \bar{\boldsymbol{A}}_{12} & \bar{\boldsymbol{B}}_{12} \\ \bar{\mathbf{0}}_{N_1\times N_2} & \bar{\mathbf{0}}_{N_1\times N_2} \end{bmatrix}, \bar{\boldsymbol{Z}}_{21}^{(1)} = \begin{bmatrix} \bar{\boldsymbol{A}}_{21} & \bar{\boldsymbol{B}}_{21} \\ \bar{\mathbf{0}}_{N_2\times N_1} & \bar{\mathbf{0}}_{N_2\times N_1} \end{bmatrix}, \tag{10}$$

where $\bar{\mathbf{0}}$ is a null matrix. The size of the matrix $\bar{\boldsymbol{Z}}$ is $2(N_1 + N_2) \times 2(N_1 + N_2)$, where N_i $(i = \{1, 2\})$ is the number of discretization points on the surface S_i of the object. The elements of the submatrices $\{\bar{\boldsymbol{A}}_{12}, \bar{\boldsymbol{B}}_{12}\}$ can be found in Appendix A.

If scatterer 2 is perfectly conducting (metallic), then $\bar{\boldsymbol{Z}}_{22} = \bar{\boldsymbol{P}}_{22}$, $\bar{\boldsymbol{Z}}_{12}^{(1)} = [\bar{\boldsymbol{P}}_{12}\ \bar{\mathbf{0}}]^{\mathrm{T}}$ and $\bar{\boldsymbol{Z}}_{21}^{(1)} = [\bar{\boldsymbol{A}}_{21}\ \bar{\boldsymbol{B}}_{21}]$, where $\bar{\boldsymbol{P}}_{ij} = \{\bar{\boldsymbol{A}}_{ij}, \bar{\boldsymbol{B}}_{ij}\}$ for the TM $(\partial\psi_2/\partial n = 0)$ and TE $(\psi_2 = 0)$ polarizations, respectively. In addition, if the scatterer 1 is perfectly conducting, then $\bar{\boldsymbol{Z}}_{12,21}^{(1)} = \bar{\boldsymbol{P}}_{12,21}$ and $\bar{\boldsymbol{Z}}_{11,22} = \bar{\boldsymbol{P}}_{11,22}$. The size of $\bar{\boldsymbol{Z}}$ is reduced to $(N_1 + N_2) \times (N_1 + N_2)$.

The excitation vector $\boldsymbol{b}$ of length $2(N_1 + N_2)$ is written as

$$\boldsymbol{b} = [\,\boldsymbol{b}_1\ \boldsymbol{b}_2\,]^{\mathrm{T}}, \tag{11}$$

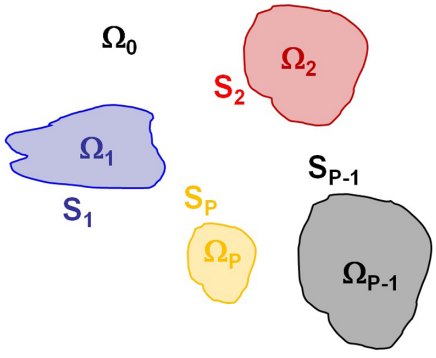

Fig. 2. Scattering from P illuminated scatterers.

where the vector $\boldsymbol{b}_i$ is defined from Eq. (2).

The unknown vector $\boldsymbol{X}$ of length $2(N_1 + N_2)$ is expressed as

$$\boldsymbol{X} = [\,\boldsymbol{X}_1\ \boldsymbol{X}_2\,]^{\mathrm{T}}, \tag{12}$$

where $\boldsymbol{X}_i$ is expressed from Eq. (3). The unknown $\boldsymbol{X}$ on $S_1 \cup S_2$ is computed from $\boldsymbol{X} = \bar{\boldsymbol{Z}}^{-1}\boldsymbol{b}$.

The scattered field $\bar{\boldsymbol{\psi}}_{\text{sca}}(\boldsymbol{r})$ in the medium $\boldsymbol{r} \in \Omega_0$ $(\boldsymbol{r} \notin S_i)$ is then obtained from the Huygens principle expressed as

$$\bar{\boldsymbol{\psi}}_{\text{sca}}(\boldsymbol{r}) = -\begin{bmatrix} \bar{\boldsymbol{P}}(\boldsymbol{r}, \boldsymbol{r}_1) \\ \bar{\boldsymbol{P}}(\boldsymbol{r}, \boldsymbol{r}_2) \end{bmatrix} \boldsymbol{X}. \tag{13}$$

If $\boldsymbol{r} \in \Omega_1$ $(\boldsymbol{r} \notin S_1)$, then the above equation is applied by taking the plus sign on the matrix $\bar{\boldsymbol{P}}(\boldsymbol{r}, \boldsymbol{r}_1)$ (instead of minus). If $\boldsymbol{r} \in \Omega_2$ $(\boldsymbol{r} \notin S_2)$, then the above equation is applied by taking the plus sign on the matrix $\bar{\boldsymbol{P}}(\boldsymbol{r}, \boldsymbol{r}_2)$.

In this paper, the formulation is generalized to P scatterers. The impedance matrix is then expressed as

$$\bar{\boldsymbol{Z}} = \begin{bmatrix} \bar{\boldsymbol{Z}}_{11} & \bar{\boldsymbol{Z}}_{12}^{(1)} & \dots & \bar{\boldsymbol{Z}}_{1P}^{(1)} \\ \bar{\boldsymbol{Z}}_{21}^{(1)} & \bar{\boldsymbol{Z}}_{22} & \dots & \bar{\boldsymbol{Z}}_{2P}^{(1)} \\ \vdots & \vdots & \ddots & \vdots \\ \bar{\boldsymbol{Z}}_{P1}^{(1)} & \bar{\boldsymbol{Z}}_{P2}^{(1)} & \dots & \bar{\boldsymbol{Z}}_{PP} \end{bmatrix}, \tag{14}$$

where $\bar{\boldsymbol{Z}}_{ii}$ is the self-impedance matrix of the scatterer i, whereas $\bar{\boldsymbol{Z}}_{ij}^{(1)}$ is the coupling matrix between the objects i and j (propagation of the scattered field from j to i) expressed from Eq. (10). The size of the matrix $\bar{\boldsymbol{Z}}$ is $N \times N$ where $N = 2\sum_{i=1}^{i=P} N_i$.

The excitation vector $\boldsymbol{b}$ of length N is written as

$$\boldsymbol{b} = [\,\boldsymbol{b}_1\ \boldsymbol{b}_2\ \dots\ \boldsymbol{b}_P\,]^{\mathrm{T}}, \tag{15}$$

where the vector $\boldsymbol{b}_i$ is defined by Eq. (2). The unknown vector $\boldsymbol{X}$ of length N is

$$\boldsymbol{X} = [\,\boldsymbol{X}_1\ \boldsymbol{X}_2 \dots \boldsymbol{X}_P\,]^{\mathrm{T}}, \tag{16}$$

where $\boldsymbol{X}_i$ is expressed from Eq. (3) and computed by solving the linear system $\bar{\boldsymbol{Z}}\boldsymbol{X} = \boldsymbol{b}$.

The scattered field $\bar{\boldsymbol{\psi}}_{\text{sca}}(\boldsymbol{r})$ in the medium $\boldsymbol{r} \in \Omega_0$ $(\boldsymbol{r} \notin S_i)$ is then obtained from the Huygens principle expressed as

$$\bar{\boldsymbol{\psi}}_{\text{sca}}(\boldsymbol{r}) = -\begin{bmatrix} \bar{\boldsymbol{P}}(\boldsymbol{r}, \boldsymbol{r}_1) \\ \bar{\boldsymbol{P}}(\boldsymbol{r}, \boldsymbol{r}_2) \\ \vdots \\ \bar{\boldsymbol{P}}(\boldsymbol{r}, \boldsymbol{r}_P) \end{bmatrix} \boldsymbol{X}. \tag{17}$$

For $\boldsymbol{r} \in \Omega_i$ $(i \neq 0$ and $\boldsymbol{r} \notin S_i)$, the above equation is applied by taking the plus sign on the matrix $\bar{\boldsymbol{P}}(\boldsymbol{r}, \boldsymbol{r}_i)$ (instead of minus).

C. Case of *P* Illuminated Scatterers Where Only One Is Illuminated

For the case of two illuminated scatterers where only one is illuminated (Fig. 3 with $P = 2$), the impedance matrix $\bar{\boldsymbol{Z}}$ is expressed as [30]

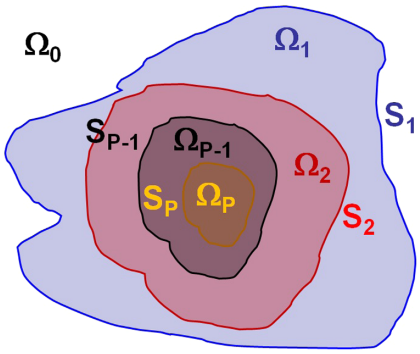

Fig. 3. P illuminated scatterers where only one is illuminated (the scatterer 1).

$$\bar{\bar{Z}} = \begin{bmatrix} \bar{\bar{Z}}_{11} & \bar{\bar{Z}}_{12}^{(2)} \\ \bar{\bar{Z}}_{21}^{(2)} & \bar{\bar{Z}}_{22} \end{bmatrix}, \tag{18}$$

where the coupling matrices $\bar{\bar{Z}}_{12}^{(2)}$ and $\bar{\bar{Z}}_{21}^{(2)}$ are written as

$$\bar{\bar{Z}}_{12}^{(2)} = \begin{bmatrix} \bar{\bar{0}}_{N_1\times N_2} & \bar{\bar{0}}_{N_1\times N_2} \\ \bar{\bar{A}}_{12} & \bar{\bar{B}}_{12} \end{bmatrix}, \bar{\bar{Z}}_{21}^{(2)} = \begin{bmatrix} \bar{\bar{A}}_{21} & \bar{\bar{D}}_{21} \\ \bar{\bar{0}}_{N_2\times N_1} & \bar{\bar{0}}_{N_2\times N_1} \end{bmatrix}, \tag{19}$$

where $\bar{\bar{0}}$ is a null matrix. The size of the matrix $\bar{\bar{Z}}$ is $2(N_1+N_2)\times 2(N_1+N_2)$. The elements of the submatrix $\bar{\bar{D}}_{21}$ can be found in Appendix A. It is important to note that the matrices $\bar{\bar{Z}}_{12}^{(2)}$ and $\bar{\bar{Z}}_{21}^{(2)}$ differ from those given by Eq. (10).

If scatterer 2 is perfectly conducting (metallic), then $\bar{\bar{Z}}_{22} = \bar{\bar{P}}_{22}$, $\bar{\bar{Z}}_{12}^{(2)} = [\bar{\bar{0}}\ \bar{\bar{P}}_{12}]^{\mathrm{T}}$ and $\bar{\bar{Z}}_{21}^{(2)} = [\bar{\bar{A}}_{21}\,\bar{\bar{D}}_{21}]$, where $\bar{\bar{P}}_{ij} = \{\bar{\bar{A}}_{ij}, \bar{\bar{B}}_{ij}\}$ for the TM ($\partial\psi_2/\partial n = 0$) and TE ($\psi_2 = 0$) polarizations, respectively. The size of $\bar{\bar{Z}}$ is reduced to $(2N_1+N_2)\times(2N_1+N_2)$.

The excitation vector $\boldsymbol{b}$ of length $2(N_1+N_2)$ is written as

$$\boldsymbol{b} = \left[\, \boldsymbol{b}_1\ \boldsymbol{0}_{1\times 2N_2} \,\right]^{\mathrm{T}}, \tag{20}$$

where the vector $\boldsymbol{b}_1$ is defined by Eq. (2). In comparison with Eq. (11), the vector $\boldsymbol{b}_2 = \boldsymbol{0}$ because, as shown in Fig. 1, the scatterer 2 is not illuminated.

The unknown vector $\boldsymbol{X}$ of length $2(N_1+N_2)$ is expressed as

$$\boldsymbol{X} = \left[\, \boldsymbol{X}_1\ \boldsymbol{X}_2 \,\right]^{\mathrm{T}}, \tag{21}$$

where $\boldsymbol{X}_i$ is expressed from Eq. (3). The unknown $\boldsymbol{X}$ on $S_1 \cup S_2$ is computed from $\boldsymbol{X} = \bar{\bar{Z}}^{-1}\boldsymbol{b}$.

The scattered field $\bar{\boldsymbol{\psi}}_{\mathrm{sca}}(\boldsymbol{r})$ in the medium $\boldsymbol{r} \in \Omega_0$ ($\boldsymbol{r} \notin S_1$) is then obtained from the Huygens principle expressed as

$$\bar{\boldsymbol{\psi}}_{\mathrm{sca}}(\boldsymbol{r}) = -\bar{\bar{P}}(\boldsymbol{r}, \boldsymbol{r}_1)\boldsymbol{X}_1. \tag{22}$$

If $\boldsymbol{r} \in \Omega_1$ ($\boldsymbol{r} \notin S_1$), then the scattered field $\bar{\boldsymbol{\psi}}_{\mathrm{sca}}(\boldsymbol{r})$ is

$$\bar{\boldsymbol{\psi}}_{\mathrm{sca}}(\boldsymbol{r}) = \begin{bmatrix} +\bar{\bar{P}}(\boldsymbol{r}, \boldsymbol{r}_1) \\ -\bar{\bar{P}}(\boldsymbol{r}, \boldsymbol{r}_2) \end{bmatrix} \boldsymbol{X}. \tag{23}$$

If $\boldsymbol{r} \in \Omega_2$ ($\boldsymbol{r} \notin S_2$), then the scattered field $\bar{\boldsymbol{\psi}}_{\mathrm{sca}}(\boldsymbol{r})$ is

$$\bar{\boldsymbol{\psi}}_{\mathrm{sca}}(\boldsymbol{r}) = \bar{\bar{P}}(\boldsymbol{r}, \boldsymbol{r}_2)\boldsymbol{X}_2. \tag{24}$$

In this paper, the formulation is generalized to P scatterers. The impedance matrix is then expressed as

$$\bar{\bar{Z}} = \begin{bmatrix} \bar{\bar{Z}}_{11} & \bar{\bar{Z}}_{12}^{(2)} & \bar{\bar{0}} & \bar{\bar{0}} & \dots & \bar{\bar{0}} \\ \bar{\bar{Z}}_{21}^{(2)} & \bar{\bar{Z}}_{22} & \bar{\bar{Z}}_{23}^{(2)} & \bar{\bar{0}} & \dots & \bar{\bar{0}} \\ \bar{\bar{0}} & \bar{\bar{Z}}_{32}^{(2)} & \bar{\bar{Z}}_{33} & \bar{\bar{Z}}_{34}^{(2)} & \dots & \bar{\bar{0}} \\ \bar{\bar{0}} & \bar{\bar{0}} & \bar{\bar{Z}}_{43}^{(2)} & \bar{\bar{Z}}_{44} & \dots & \bar{\bar{0}} \\ \vdots & \vdots & \ddots & \ddots & \bar{\bar{Z}}_{P-1,P-1} & \bar{\bar{Z}}_{P-1,P}^{(2)} \\ \bar{\bar{0}} & \bar{\bar{0}} & \dots & \bar{\bar{0}} & \bar{\bar{Z}}_{P,P-1}^{(2)} & \bar{\bar{Z}}_{PP} \end{bmatrix}, \tag{25}$$

where $\bar{\bar{Z}}_{ii}$ (or $\bar{\bar{Z}}_{i,i}$) is the self-impedance matrix of the scatterer i, whereas $\bar{\bar{Z}}_{ij}^{(2)}$ (or $\bar{\bar{Z}}_{i,j}^{(2)}$) is the coupling matrix between the objects i and j (propagation of the scattered field from j to i) expressed from Eq. (19). Unlike the matrix expressed in Eq. (18), Eq. (25) shows that only two adjacent scatterers i and $\min(|i+1|, P)$ interact, which explains why null matrices appear.

The excitation vector $\boldsymbol{b}$ is given by

$$\boldsymbol{b} = \left[\, \boldsymbol{b}_1\ \boldsymbol{0}_{\left[1\times 2\sum_{i=2}^{i=P} N_i\right]} \,\right]^{\mathrm{T}}. \tag{26}$$

It differs from Eq. (15) because $\boldsymbol{b}_i = \boldsymbol{0}$ for $i \in [2;\ P]$ (these scatterers are not illuminated).

The unknown vector $\boldsymbol{X}$ of length $N = 2\sum_{i=1}^{i=P} N_i$ is expressed from Eq. (16) and computed by solving the linear system $\bar{\bar{Z}}\boldsymbol{X} = \boldsymbol{b}$.

The scattered field $\bar{\boldsymbol{\psi}}_{\mathrm{sca}}(\boldsymbol{r})$ in the medium $\boldsymbol{r} \in \Omega_0$ ($\boldsymbol{r} \notin S_1$) is obtained from the Huygens principle given by Eq. (24). For $\boldsymbol{r} \in \Omega_i$ ($i \in [1;\ P-1]$, $\boldsymbol{r} \notin (S_i \cup S_{i+1})$), the scattered field is

$$\bar{\boldsymbol{\psi}}_{\mathrm{sca}}(\boldsymbol{r}) = \begin{bmatrix} +\bar{\bar{P}}(\boldsymbol{r}, \boldsymbol{r}_i) \\ -\bar{\bar{P}}(\boldsymbol{r}, \boldsymbol{r}_{i+1}) \end{bmatrix} \begin{bmatrix} \boldsymbol{X}_i \\ \boldsymbol{X}_{i+1} \end{bmatrix}. \tag{27}$$

For $\boldsymbol{r} \in \Omega_P$ ($\boldsymbol{r} \notin S_P$), the scattered field is $\bar{\boldsymbol{\psi}}_{\mathrm{sca}}(\boldsymbol{r}) = \bar{\bar{P}}(\boldsymbol{r}, \boldsymbol{r}_P)\boldsymbol{X}_P$.

D. Combination of Cases

As an example, in this paragraph, the impedance matrix of the scenario presented in Fig. 4 is determined. It is expressed as

$$\bar{\bar{Z}} = \begin{bmatrix} \bar{\bar{Z}}_{11} & \bar{\bar{Z}}_{12}^{(1)} & \bar{\bar{Z}}_{13}^{(1)} & \bar{\bar{0}} & \bar{\bar{0}} \\ \bar{\bar{Z}}_{21}^{(1)} & \bar{\bar{Z}}_{22} & \bar{\bar{Z}}_{23}^{(1)} & \bar{\bar{0}} & \bar{\bar{0}} \\ \bar{\bar{Z}}_{31}^{(1)} & \bar{\bar{Z}}_{32}^{(1)} & \bar{\bar{Z}}_{33} & \bar{\bar{Z}}_{34}^{(2)} & \bar{\bar{Z}}_{35}^{(2)} \\ \bar{\bar{0}} & \bar{\bar{0}} & \bar{\bar{Z}}_{43}^{(2)} & \bar{\bar{Z}}_{44} & \bar{\bar{Z}}_{45}^{(1)} \\ \bar{\bar{0}} & \bar{\bar{0}} & \bar{\bar{Z}}_{53}^{(2)} & \bar{\bar{Z}}_{54}^{(1)} & \bar{\bar{Z}}_{55} \end{bmatrix}. \tag{28}$$

The impedance matrix of scatterers 1, 2, and 3 is expressed from Eq. (14), with $P = 3$. This explains the first three rows and columns of $\bar{\bar{Z}}$ with the superscript (1) (Case 1). The impedance matrix of scatterers 4 and 5 is expressed from Eq. (9), in which the subscripts {1, 2} are replaced by {4, 5}, and the incident medium is Ω_3. This explains the last two rows and columns of $\bar{\bar{Z}}$ with the superscript (1) (Case 1). The impedance matrix of scatterers 3 and 4 union 5 is expressed from Eq. (18). This explains the rows (4,5) and columns (4,5) of $\bar{\bar{Z}}$ with the superscript (2)

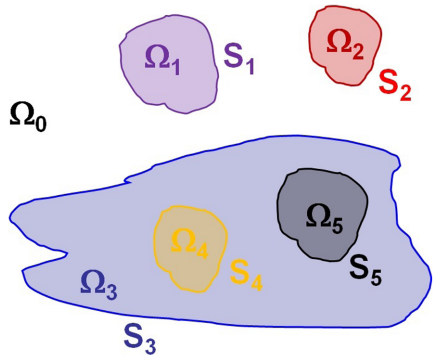

Fig. 4. Combination of cases.

(Case 2). The eight null matrices appear because scatterers 1 and 2 do not directly interact with objects 4 and 5.

The excitation vector $\boldsymbol{b}$ is given by

$$\boldsymbol{b} = \left[\, \boldsymbol{b}_1 \;\; \boldsymbol{b}_2 \;\; \boldsymbol{b}_3 \;\; \boldsymbol{0}_{1\times 2(N_4+N_5)} \,\right]^{\mathrm{T}}, \tag{29}$$

for which the scatterers 4 and 5 are not illuminated. It is important to note that, if a source exists in the medium Ω_3, then $\boldsymbol{b}_4$ and $\boldsymbol{b}_5$ differ from $\boldsymbol{0}$. By inverting the matrix $\boldsymbol{Z}$, the surface currents on the surfaces $\{S_{i\in[1;\,P]}\}$ are computed.

The scattered field $\bar{\boldsymbol{\psi}}_{\mathrm{sca}}(\boldsymbol{r})$ in the medium $\boldsymbol{r}\in\Omega_0$ ($\boldsymbol{r}\notin(S_1\cup S_2\cup S_3)$) is then obtained from the Huygens principle expressed as

$$\bar{\boldsymbol{\psi}}_{\mathrm{sca}}(\boldsymbol{r}) = -\begin{bmatrix} \bar{\boldsymbol{P}}(\boldsymbol{r},\,\boldsymbol{r}_1) \\ \bar{\boldsymbol{P}}(\boldsymbol{r},\,\boldsymbol{r}_2) \\ \bar{\boldsymbol{P}}(\boldsymbol{r},\,\boldsymbol{r}_3) \end{bmatrix} \begin{bmatrix} \boldsymbol{X}_1 \\ \boldsymbol{X}_2 \\ \boldsymbol{X}_3 \end{bmatrix}. \tag{30}$$

For $\boldsymbol{r}\in\Omega_3$ ($\boldsymbol{r}\notin(S_3\cup S_4\cup S_5)$), the scattered field is

$$\bar{\boldsymbol{\psi}}_{\mathrm{sca}}(\boldsymbol{r}) = \begin{bmatrix} +\bar{\boldsymbol{P}}(\boldsymbol{r},\,\boldsymbol{r}_1) \\ -\bar{\boldsymbol{P}}(\boldsymbol{r},\,\boldsymbol{r}_4) \\ -\bar{\boldsymbol{P}}(\boldsymbol{r},\,\boldsymbol{r}_5) \end{bmatrix} \begin{bmatrix} \boldsymbol{X}_1 \\ \boldsymbol{X}_4 \\ \boldsymbol{X}_5 \end{bmatrix}. \tag{31}$$

For $\boldsymbol{r}\in\Omega_4$ ($\boldsymbol{r}\notin S_4$), $\bar{\boldsymbol{\psi}}_{\mathrm{sca}}(\boldsymbol{r}) = \bar{\boldsymbol{P}}(\boldsymbol{r},\,\boldsymbol{r}_4)\boldsymbol{X}_4$. For $\boldsymbol{r}\in\Omega_5$ ($\boldsymbol{r}\notin S_5$), $\bar{\boldsymbol{\psi}}_{\mathrm{sca}}(\boldsymbol{r}) = \bar{\boldsymbol{P}}(\boldsymbol{r},\,\boldsymbol{r}_5)\boldsymbol{X}_5$.

In conclusion, the two cases presented in the previous sections allow us to generalize to any configuration made up of P scatterers. To construct the impedance matrix, the following method is proposed.

For a given scenario, first a boolean interaction matrix $\bar{\boldsymbol{M}}$ of size $P\times P$ is built. If the scatterer j shares a medium Ω_j with the scatterer i, then $M_{ij}=1$, 0 otherwise. For the case presented in Fig. 4, $\bar{\boldsymbol{M}}$ is written as

$$\bar{\boldsymbol{M}} = \begin{bmatrix} 1 & 1 & 1 & 0 & 0 \\ 1 & 1 & 1 & 0 & 0 \\ 1 & 1 & 1 & 1 & 1 \\ 0 & 0 & 1 & 1 & 1 \\ 0 & 0 & 1 & 1 & 1 \end{bmatrix}. \tag{32}$$

If $M_{ij}=0$, then the corresponding matrix $\bar{\boldsymbol{Z}}_{ij}=\bar{\boldsymbol{0}}$. The matrix $\bar{\boldsymbol{M}}$ is symmetric, owing to the reciprocity principle, and $M_{ii}=1 \quad \forall\, i\in[1;\,P]$.

Second, to distinguish cases of Figs. 2 and 3, for $M_{ij}=1$, if the scatterer j has its surrounding medium $\Omega_{i\neq j,i\neq 0}$ belonging to the medium Ω_i of the scatterer i, then $M_{ij}=2$ [case of Fig. 3, coupling matrix with the superscript (2)], 1 otherwise [case of Fig. 2, coupling matrix with the superscript (1)]. Equation (33) becomes

$$\bar{\boldsymbol{M}} = \begin{bmatrix} 1 & 1 & 1 & 0 & 0 \\ 1 & 1 & 1 & 0 & 0 \\ 1 & 1 & 1 & 2 & 2 \\ 0 & 0 & 2 & 1 & 1 \\ 0 & 0 & 2 & 1 & 1 \end{bmatrix}. \tag{33}$$

In conclusion, if $M_{ij}=0$ then $\bar{\boldsymbol{Z}}_{ij}=\bar{\boldsymbol{0}}$, $\bar{\boldsymbol{Z}}_{ij}=\bar{\boldsymbol{Z}}_{ij}^{(m_{ij})}$ $(i\neq j)$ otherwise. For the excitation vector $\boldsymbol{b}$, if the source belongs to the medium $\Omega_{i\in[0;\,P]}$, then the scatterer set $J=\{j\}$ that shares this medium is illuminated. This means that $\boldsymbol{b}'_J=\psi_{\mathrm{inc}}(\boldsymbol{r}\in S_J)$, $\boldsymbol{b}'_{\bar{J}}=\bar{\boldsymbol{0}}_{1\times\sum N_{\bar{J}}}$ otherwise, where $\bar{J}=J\notin[1;\,P]$. The scattered field in medium $\Omega_{i\in[0;\,P]}$ is computed by using the same methods as those previously addressed.

3. CHARACTERISTIC BASIS FUNCTION METHOD

For P dielectric scatterers, the size of the matrix to be inverted is $N\times N$, where $N=2\sum_{i=1}^{i=P}N_i$. The direct solution of the linear system $\bar{\boldsymbol{Z}}\boldsymbol{X}=\boldsymbol{b}$ through a direct lower upper (LU) decomposition is usually limited by $\mathcal{O}(N^3)$ and $\mathcal{O}(N^2)$ complexities in CPU time and memory requirement, respectively. This is computationally expensive for an electrically large multiscale object or a collection of dielectric objects (i.e., N huge). To tackle this issue, the domain decomposition method, named the characteristic basis function method (CBFM), is applied. A summary of this method can be found in [44,45].

It is important to note that, originally, the CBFM was developed for radiation and 3D scattering problems [44] and on a single geometry. Next, it was extended to a single and two 3D dielectric scatterers [40,43].

For a 2D problem, some minor changes are needed.

A. Case of Metallic Scatterers

First, the scatterers are assumed to be metallic. The CBFM begins by dividing the geometry of the problem to be analyzed into B blocks, where $\bar{\boldsymbol{Z}}_{i,i}$ is the self-impedance matrix of the block i. Next, a primary basis function (PBF), $\boldsymbol{Y}_{i',k_{\mathrm{IPW}}}$, is computed for each block by solving the linear system

$$\bar{\boldsymbol{Z}}_{i',i'}\boldsymbol{Y}_{i',k_{\mathrm{IPW}}} = \boldsymbol{B}_{i',k_{\mathrm{IPW}}}, \tag{34}$$

where the subscript prime indicates that the block i is enlarged and k_{IPW} stands for the k_{IPW}th plane wave (ranging from 1 to $N_{\mathrm{IPW},i}$). The original version of CBFM [44] used $\boldsymbol{B}_{i',k_{\mathrm{IPW}}}=\boldsymbol{b}_{i'}$ (single incident plane wave, $k_{\mathrm{IPW}}=1$), and the secondary basis functions (SBFs) are calculated. In 2008 [48], a more efficient way is proposed to calculate the PBFs, and the computation of SBFs is not required.

Lucente *et al.* [48] solved the linear system in Eq. (34) from a collection of $N_{\mathrm{IPW},i}$ incident plane waves $\{\boldsymbol{B}_{i',k_{\mathrm{IPW}}}\}$, and the resulting vectors $\{\boldsymbol{Y}_{i',k_{\mathrm{IPW}}}\}$ are stored in a matrix $\bar{\boldsymbol{J}}_i$ of size $N_i\times N_{\mathrm{IPW},i}$, where N_i is the number of unknowns of the

block i without overlapping. This means that the overlapped unknowns of $\boldsymbol{Y}_{i',k_{\mathrm{IPW}}}$ are removed.

The choice of $N_{\mathrm{IPW},i}$ must be relevant to avoid the size of the matrix being too big. The redundant information due to the overestimation of $N_{\mathrm{IPW},i}$ is eliminated via the use of a truncated singular value decomposition (SVD). This means that, from a given threshold $\epsilon_{\mathrm{CBFM,SVD}}$, the values for which the modulii of the normalized eigenvalues are smaller than $\epsilon_{\mathrm{CBFM,SVD}}$ are removed. The size of $\bar{\boldsymbol{J}}_{\boldsymbol{i}}$ becomes $N_i \times N_{\mathrm{IPW,SVD},i}$, with $N_{\mathrm{IPW,SVD},i} < N_{\mathrm{IPW},i}$.

The last stage of CBFM consists in solving a reduced linear system $\bar{\boldsymbol{Z}}^{\mathrm{R}}\boldsymbol{a}^{\mathrm{R}} = \boldsymbol{b}^{\mathrm{R}}$ defined as

$$\begin{bmatrix} \bar{\boldsymbol{Z}}^{\mathrm{R}}_{1,1} & \bar{\boldsymbol{Z}}^{\mathrm{R}}_{1,2} & \cdots & \bar{\boldsymbol{Z}}^{\mathrm{R}}_{1,B} \\ \bar{\boldsymbol{Z}}^{\mathrm{R}}_{2,1} & \bar{\boldsymbol{Z}}^{\mathrm{R}}_{2,2} & \cdots & \bar{\boldsymbol{Z}}^{\mathrm{R}}_{2,B} \\ \vdots & \vdots & \ddots & \vdots \\ \bar{\boldsymbol{Z}}^{\mathrm{R}}_{B,1} & \bar{\boldsymbol{Z}}^{\mathrm{R}}_{B,2} & \cdots & \bar{\boldsymbol{Z}}^{\mathrm{R}}_{B,B} \end{bmatrix} \begin{bmatrix} \boldsymbol{a}^{\mathrm{R}}_1 \\ \boldsymbol{a}^{\mathrm{R}}_2 \\ \vdots \\ \boldsymbol{a}^{\mathrm{R}}_B \end{bmatrix} = \begin{bmatrix} \boldsymbol{b}^{\mathrm{R}}_1 \\ \boldsymbol{b}^{\mathrm{R}}_2 \\ \vdots \\ \boldsymbol{b}^{\mathrm{R}}_B \end{bmatrix}, \tag{35}$$

where the submatrix $\bar{\boldsymbol{Z}}^{\mathrm{R}}_{i,j}$ and the subvector $\boldsymbol{b}^{\mathrm{R}}_i$ are defined as

$$\begin{cases} \bar{\boldsymbol{Z}}^{\mathrm{R}}_{i,j} = \bar{\boldsymbol{J}}^{\mathrm{H}}_i \bar{\boldsymbol{Z}}_{i,j} \bar{\boldsymbol{J}}_j & \left[N_{\mathrm{IPW,SVD},i} \times N_{\mathrm{IPW,SVD},j}\right] \\ \boldsymbol{b}^{R}_j = \bar{\boldsymbol{J}}^{\mathrm{H}}_j \boldsymbol{b}_j & \left[N_{\mathrm{IPW,SVD},i} \times 1\right] \end{cases}. \tag{36}$$

Moreover, the symbol H stands for the conjugate transpose operator, and the indexes i and j range from 1 to B. The unknown vector $\boldsymbol{X}_i$ of the block i equals $\boldsymbol{X}_i = \bar{\boldsymbol{J}}_i \boldsymbol{a}^R_i$.

The problem is then represented by the characteristic square matrix of size $(B\bar{N}_{\mathrm{IPW,SVD}})^2$ instead of a square matrix of size $N^2 = (B\bar{N})^2$, where $\bar{N} = (1/B)\sum_{p=1}^{B} N_i$ and $\bar{N}_{\mathrm{IPW,SVD}} = (1/B)\sum_{p=1}^{B} N_{\mathrm{IPW,SVD},p}$ (mean values over the number of blocks B). Then, the reduction factor is $(\bar{N}/\bar{N}_{\mathrm{IPW,SVD}})^2$. If multiple excitations $\{\boldsymbol{b}\}$ (for instance, monostatic case) are considered, then the storing of $\bar{\boldsymbol{Z}}^{\mathrm{R}}$ avoids to repeat the procedure, and the surface currents are calculated rapidly. The complexity of CBFM is detailed in [45].

Originally, the CBFM splits up the single geometry into B blocks, since for a 3D problem the number of unknowns can be huge. In this paper, since the number of unknowns N_i of a single scatterer is moderate, it is not required to decompose it into blocks, but it is not a limitation. This means that the number of blocks equals the number of scatterers, $B = P$, and that the overlapping between the scatterers is not necessary.

B. Case of Dielectric Scatterers

As shown by Eq. (1), for a dielectric scatterer, the self-impedance matrix of size $2N_i \times 2N_i$ is expressed from four submatrices of size $N_i \times N_i$. Thus, the PFBs are calculated by repeating the procedure four times used for a metallic object and illustrated by Eq. (34). This leads to the matrix

$$\bar{\boldsymbol{J}}_i = \begin{bmatrix} \bar{\boldsymbol{J}}_{i,11} & \bar{\boldsymbol{J}}_{i,12} \\ \bar{\boldsymbol{J}}_{i,21} & \bar{\boldsymbol{J}}_{i,22} \end{bmatrix}, \tag{37}$$

where the submatrices $\{\bar{\boldsymbol{J}}_{i,pq}\}$ $(p = \{1,2\},\ q = \{1,2\})$ are obtained from the four submatices of $\bar{\boldsymbol{Z}}_{i',i'}$, i.e., $\{\bar{\boldsymbol{A}}_{i',i'}, \bar{\boldsymbol{B}}_{i',i'}, \bar{\boldsymbol{C}}_{i',i'}, \bar{\boldsymbol{D}}_{i',i'}\}$. This representation implies that the numbers of plane waves $\{N_{\mathrm{IPW},i,pq}\}$ of $\{\bar{\boldsymbol{J}}_{i,pq}\}$ satisfy $N_{\mathrm{IPW},i,11} = N_{\mathrm{IPW},i,21}$ and $N_{\mathrm{IPW},i,12} = N_{\mathrm{IPW},i,22}$. This means that the size of $\bar{\boldsymbol{J}}_i$ is $2N_i \times (N_{\mathrm{IPW},i,11} + N_{\mathrm{IPW},i,12})$. Like a metallic scatterer, the redundant information is eliminated via the use of a truncated singular value decomposition (SVD). This yields that the new size of $\bar{\boldsymbol{J}}_i$ is $2N_i \times N_{i,\mathrm{IPW}}$, with $N_{i,\mathrm{IPW}} < N_{\mathrm{IPW},i,11} + N_{\mathrm{IPW},i,12}$. Equations (35) and (36) are unchanged.

The SVD decomposition can be applied on each submatrices $\bar{\boldsymbol{J}}_{i,pq}$, and the resulting compressed matrix $\bar{\boldsymbol{J}}_i$ is obtained from Eq. (37). Numerical tests revealed that this procedure has a lower precision than when the SVD is applied on the whole matrix $\bar{\boldsymbol{J}}_i$.

For convenience, Table 1 lists the notations introduced in this paper.

Table 1. Notations Introduced in This Paper

Name	Definition
P	Number of scatterers
B	Number of blocks $(= P)$
N	Total number of unknowns
N_i	Number of unknowns of scatterer i
$N_{\mathrm{IPW},p}$	CBFM plane wavenumber of block i
$N_{\mathrm{IPW,SVD},p}$	CBFM plane wavenumber of block i after SVD truncation
$\epsilon_{\mathrm{CBFM,SVD}}$	CBFM threshold of the SVD truncation
$\bar{N}$	Mean value of N_i over $p \in [1;\ B]$
$\bar{N}_{\mathrm{IPW}}$	Mean value of $N_{\mathrm{IPW},i}$ over $i \in [1;\ B]$
$\bar{N}_{\mathrm{IPW,SVD}}$	Mean value of $N_{\mathrm{IPW,SVD},i}$ over $i \in [1;\ B]$

4. CBFM COMBINED WITH THE KIRCHOFF APPROXIMATION

For a given plane wave $\boldsymbol{B}_{i',k_{\mathrm{IPW}}}$, the calculation of a PBF, $\boldsymbol{Y}_{i',k_{\mathrm{IPW}}}$, requires solving the linear system $\bar{\boldsymbol{Z}}_{i',i'}\boldsymbol{Y}_{i',k_{\mathrm{IPW}}} = \boldsymbol{B}_{i',k_{\mathrm{IPW}}}$, leading to a complexity of $\mathcal{O}(N^3_{i'})$, where $N_{i'}$ is the number of unknowns with overlapping. To reduce the complexity of this operation to $\mathcal{O}(N_i)$, the Kirchoff approximation (KA) is applied.

For a dielectric scatterer of surface S separating two homogeneous media (Ω_1, Ω_2), the surface current and its normal derivative on $\boldsymbol{r} \in S$ are expressed as [49,50]

$$\begin{cases} \psi(\boldsymbol{r}) = [1 + \mathcal{R}(\theta)]\ \psi_{\mathrm{inc}}(\boldsymbol{r})\mathcal{I}(\boldsymbol{r}) \\ \frac{\partial\psi(\boldsymbol{r})}{\partial n} = [1 - \mathcal{R}(\theta)]\ \frac{\partial\psi_{\mathrm{inc}}(\boldsymbol{r})}{\partial n}\mathcal{I}(\boldsymbol{r}) \end{cases}, \tag{38}$$

where $\mathcal{R}$ is the Fresnel reflection coefficient defined as

$$\mathcal{R} = \begin{cases} \frac{n_2\cos\theta - n_1\cos\theta_t}{n_2\cos\theta + n_1\cos\theta_t} & \text{TM polarization} \\ \frac{n_1\cos\theta - n_2\cos\theta_t}{n_1\cos\theta + n_2\cos\theta_t} & \text{TE polarization} \end{cases}. \tag{39}$$

In addition, $\cos\theta = -\hat{\boldsymbol{k}}_{\mathrm{inc}} \cdot \hat{\boldsymbol{n}}$, $\cos\theta_t = \sqrt{1 - n_1^2(1 - \cos^2\theta)/n_2^2}$, and $n_i = \sqrt{\epsilon_{r,i}}$ $(i = \{1,2\})$ the refraction index of the medium Ω_i. The unitary vector $\hat{\boldsymbol{k}}_{\mathrm{inc}}$ stands for the incident direction, and $\hat{\boldsymbol{n}}$ is the unitary vector normal to the surface at the point $\boldsymbol{r}$. In Eq. (38), $\mathcal{I}(\boldsymbol{r})$ denotes a boolean illumination function. If a point on the surface $\boldsymbol{r} \in S$ is viewed (that is, $\cos\theta \geq 0$) by the transmitter, then $\mathcal{I}(\boldsymbol{r}) = 1$; 0 otherwise.

For a metallic surface, $\mathcal{R}=\{+1,-1\}$ for the TM and TE polarizations, respectively. This leads to $\{\psi = 2\mathcal{I}\psi_{\rm inc}, \partial\psi/\partial n = 0\}$ for TM and to $\{\psi = 0, \partial\psi/\partial n = 2\mathcal{I}\partial\psi_{\rm inc}/\partial n\}$ for TE.

Assuming a plane incident wave $\psi_{\rm inc} = e^{j\boldsymbol{k}_{\rm inc}\cdot\boldsymbol{r}}$, Eq. (38) becomes

$$\begin{cases} \psi(\boldsymbol{r}) = [1+\mathcal{R}(\theta)]\, e^{j\boldsymbol{k}_{\rm inc}\cdot\boldsymbol{r}}\mathcal{I}(\boldsymbol{r}) \\ \frac{\partial\psi(\boldsymbol{r})}{\partial n} = [1-\mathcal{R}(\theta)]\, e^{j\boldsymbol{k}_{\rm inc}\cdot\boldsymbol{r}}\mathcal{I}(\boldsymbol{r})\, j\boldsymbol{k}_{\rm inc}\cdot\hat{\boldsymbol{n}} \end{cases}. \tag{40}$$

In Eq. (37), the PBFs $\{\bar{\boldsymbol{J}}_{i,11}, \bar{\boldsymbol{J}}_{i,12}\}$ are obtained from Eq. (40) by taking $\mathcal{R}=\{+1,-1\}$ (metallic case), respectively, whereas $\{\bar{\boldsymbol{J}}_{i,21}, \bar{\boldsymbol{J}}_{i,22}\}$ are obtained from Eq. (40).

In other words, it is equivalent to write that $\bar{\boldsymbol{Z}}_{i,i}$ is a diagonal matrix (because only local interactions are accounted for, that is, the multiple reflections are neglected) by blocks. The two upper blocks have N_i elements equal to $2\mathcal{I}(\boldsymbol{r}_m)$ and $2\mathcal{I}(\boldsymbol{r}_m)\boldsymbol{k}_{\rm inc}\cdot\hat{\boldsymbol{n}}_m$, respectively, whereas the two lower blocks have N_i elements equal to $\mathcal{I}(\boldsymbol{r}_m)[1+\mathcal{R}(\theta_m)]$ (θ_m depends on $\boldsymbol{r}_m$ discretized on S) and $\mathcal{I}(\boldsymbol{r}_{\mathbf{m}})[1-\mathcal{R}(\theta_m)]j\boldsymbol{k}_{\rm inc}\cdot\hat{\boldsymbol{n}}_m$, respectively.

To calculate the PBFs with KA, the resulting complexity is $\mathcal{O}(N_i)$ instead of $\mathcal{O}(N_{i'}^3)$ from a conventional LU decomposition. For the numerical results, keep in mind that there is no overlapping between the $P=B$ scatterers, meaning that $N_{i'}=N_i$.

5. NUMERICAL RESULTS

In this section, numerical examples are exhibited to demonstrate the efficiency of CBFM combined with either LU or KA for the calculation of the PBFs. Table 2 lists parameters of the four scenarios.

A. Scenario 1: Stack of Rough Interfaces

First, the scattering from a stack of $P=6$ random rough interfaces separating homogeneous media is considered. Table 3 lists the simulation parameters; Fig. 5 shows the scenario.

To attenuate the edge diffraction by the upper surface, Thorsos's [51] Gaussian-tapered incident wave is applied with $g = L_1/6 = 10\lambda_0$, and the incident angle is $\theta_{\rm inc}=0$. The parameter g controls the extend of the incident wave.

To calculate the PBFs, the incident waves [vectors $\{\boldsymbol{B}_{i',k_{\rm IPW}}\}$ in Eq. (34)] are assumed to be plane, and their incidence angles range from 0 to 2π. In addition, they are spaced equally and their number, $N_{\rm IPW}$, is assumed to be

$$N_{\rm IPW} = \left\lfloor \frac{k_0 D+1}{n_{\rm IPW}} \right\rfloor, \tag{41}$$

Table 2. Parameters of the Four Scenarios[a]

Scenario	$\epsilon_{\rm CBFM,SVD}$	N	N_R	$N_{R,\rm SVD}$	$t_{\rm LU}$	$t_{\rm CBFM-LU}$	$t_{\rm CBFM-KA}$
1	10^{-4}	14,400	4,392	2,925	98	20	16
2	10^{-5}	4,074	1096	1036	15	0.6	0.5
3	10^{-4}	11,436	3,336	2,168	48	5	4
4	10^{-5}	11,056	3,326	2,690	81	13	11

[a]See Table 1 for the notations. In addition, computing times of LU (applied on the entire matrix) $t_{\rm LU}$, CBFM-LU, $t_{\rm CBFM-LU}$, and CBFM-KA, $t_{\rm CBFM-KA}$ in seconds. The matrix filling time is included.

Table 3. Parameters of the First Scenario: A Stack of $P=6$ Random Rough Interfaces Separating Homogeneous Media Ω_i of Permittivity $\epsilon_{r,i}$[a]

Medium Ω_i	$\epsilon_{r,i}$	Scatterer i	$\sigma_{z,i}[\lambda_0]$	$L_{c,i}[\lambda_0]$	$h_i[\lambda_0]$
0	1				
1	$2+0.01j$	1	0.1	1	0
2	$2.5+0.02j$	2	0.15	1.5	−2
3	$3+0.03j$	3	0.2	2	−4
4	$2+0.01j$	4	0.1	1	−6
5	$2.5+0.02j$	5	0.15	1.5	−8
6	$3+0.03j$	6	0.2	2	−10

[a]The rough surface number i obeys a Gaussian height distribution with a height autocorrelation function (ACF) assumed to be Gaussian, with a standard deviation $\sigma_{z,i}$ and a correlation length $L_{c,i}$. Its height mean value (or depth) is h_i, the surface lengths are equal to $60\lambda_0$, where λ_0 is the wavelength in vacuum (medium Ω_0), and the sampling step per wavelength λ_0 is equal to 20.

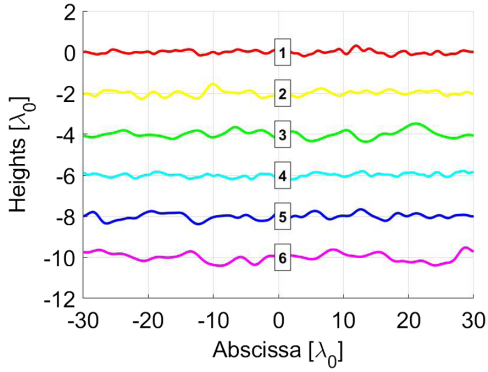

Fig. 5. Scenario 1: A stack of $P=6$ rough interfaces separating homogeneous media. The simulation parameters are listed in Table 3.

where the symbol $\lfloor$ stands for the upper integer part, D the largest dimension of the scatterer, and $k_0 = 2\pi/\lambda_0$ the wavenumber in vacuum. For $n_{\rm IPW}=1$, the above equation gives the number of eigen modes that contribute to the scattering from a circular cylinder of diameter D. Since for a rough surface, $N_{\rm IPW}$ is overestimated, the number $n_{\rm IPW}>1$ is introduced.

Figure 6 plots the modulus of the surface currents $\{\psi_1, \psi_6\}$ (upper and lower interfaces) in dB scale versus the surface abscissa. In the legend, the labels mean "CBFM($\epsilon_{\rm CBFM,SVD}$-$n_{\rm IPW}$)-LU: $\bar{N}_{\rm IPW} - \bar{N}_{\rm IPW,SVD}$, RRE" (Table 1), where the relative residual error (RRE) is defined as

$$\text{RRE} = \frac{\text{norm}\,(\boldsymbol{X}_{\rm LU} - \boldsymbol{X}_{\rm CBFM})}{\text{norm}\,(\boldsymbol{X}_{\rm LU})}. \tag{42}$$

The norm is the norm 2, which is calculated over the surface abscissa x_i. CBFM-LU means that the PBFs are computed from a LU decomposition. In addition, the legend "LU" means that the strengths are computed from the brute force MoM (LU decomposition of the entire matrix of the problem, that is, the reference solution).

As we can see, for $n_{\rm IPW}=3$, the results match well with those obtained from LU, and the comparison is better for $\epsilon_{\rm CBFM,SVD}=10^{-4}$, as expected, but the number $\bar{N}_{\rm IPW,SVD}$ is larger. Table 2 shows that the size of the reduced matrix is 4.9 times smaller than that of the entire problem and the gain in

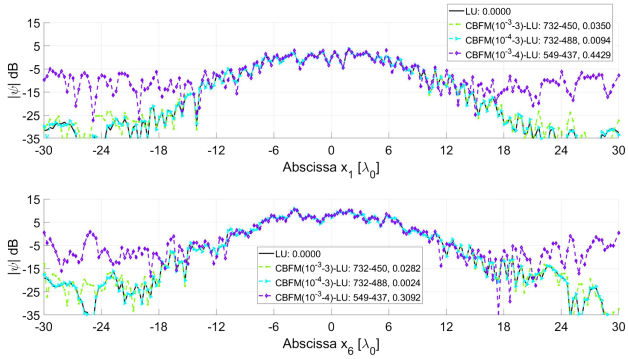

Fig. 6. Modulus of the surface current currents $\{\psi_1, \psi_6\}$ (upper and lower interfaces) in dB scale versus the surface abscissa (scenario depicted in Fig. 5). The polarization is TM.

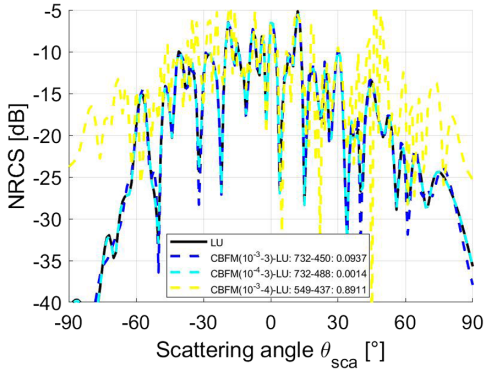

Fig. 7. NRCS in dB scale versus the scattering angle θ_{sca} (scenario depicted in Fig. 5). The polarization is TM.

saving time is of the order of 5. Figure 6 also shows that, for $n_{\text{IPW}} = 4$, the results do not coincide with those of LU.

Figure 7 plots the NRCS in dB scale versus the scattering angle θ_{sca} (scenario depicted in Fig. 5). The polarization is TM. RRE is calculated over the scattering angles θ_{sca} of the field scattered by the upper surface (scatterer 1). As we can see, for $n_{\text{IPW}} = 3$, a good agreement is obtained between CBFM and LU, and, for $n_{\text{IPW}} = 4$, the disagreement is strong.

Figure 8 plots the same variations as in Fig. 7, but the PBFs are computed from LU and KA with $n_{\text{IPW}} = 3$. As we can see, for $\epsilon_{\text{CBFM,SVD}} = 10^{-5}$, CBFM-KA predicts satisfactory results, whereas those obtained from CBFM-LU are very good for $\epsilon_{\text{CBFM,SVD}} = 10^{-4}$. However, for $\epsilon_{\text{CBFM,SVD}} = 10^{-6}$, the difference between LU and CBFM-KA is small. This means that, for a given threshold $\epsilon_{\text{CBFM,SVD}}$, $\bar{N}_{\text{IPW,SVD}}$ of KA is smaller than that of LU, and, to obtain a similar value between KA and LU, $\epsilon_{\text{CBFM,SVD}}$ of KA has to decrease. In other words, the eigenvalue spectrum of PBFs of KA is broader than that of LU. It is important to point out that KA allows us to accelerate the computation of the PBFs because no inversion is needed, unlike LU.

The Kirchoff approximation is valid if the mean surface curvature radius R_c is greater than the electromagnetic wavelength [49] (the term $\cos^3\theta$ is omitted). For a Gaussian ACF [52,53], $R_c \approx L_c^2(1 + 1.5\sigma_z/L_c)/(2.76\sigma_z) \approx \{4.16, 6.25, 8.33, 4.16, 6.25, 8.33\}\lambda_0$ for the surfaces depicted

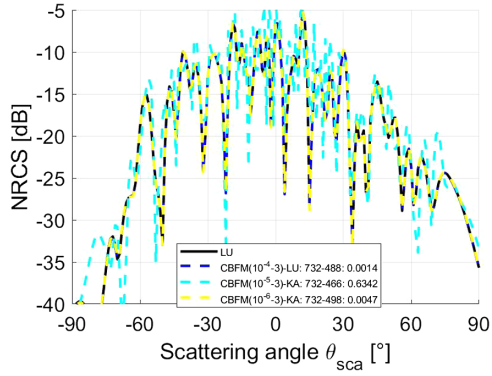

Fig. 8. NRCS in dB scale versus the scattering angle θ_{sca} (scenario depicted in Fig. 5). The PBFs are computed from LU and KA, with $n_{\text{IPW}} = 3$.

in Fig. 5. Numerical results, not depicted in the paper, demonstrate that, when $R_c < \lambda_0$, the precision of CBFM-KA is lower. In addition, it is important to underline that the multiple reflections are neglected with KA, which implies that the surface RMS slope must be moderate (typically, smaller than 0.3–0.35).

Figure 9 plots the same variations as in Fig. 7, but the polarization is TE. For LU, $\epsilon_{\text{CBFM,SVD}} = 10^{-4}$, whereas for KA, $\epsilon_{\text{CBFM,SVD}} = 10^{-6}$. As we can see, a good agreement is obtained with LU, which implies that the input parameters are well chosen.

This first study showed that, for a stack of rough interfaces, the CBFM combined with either LU or KA gives very good results. To calculate the PBFs, Eq. (41) with $n_{\text{IPW}} = 3$ slightly overestimates the number of incident plane waves. The use of a SVD truncation allows us to reduce this number by a factor ranging from 1.5 to 1.6 (see Table 2 or legends of Figs. 7–9), which implies that the size of the reduced matrix also decreases. It is also important to underline that the threshold $\epsilon_{\text{CBFM,SVD}}$ must be divided by 100 for KA in comparison with LU (with $\epsilon_{\text{CBFM,SVD}} = 10^{-4}$) to obtain a similar value of $\bar{N}_{\text{IPW,SVD}}$.

B. Scenario 2: Collection of Elliptical Cylinders

In this subsection, the scattering from a collection of 21 elliptical dielectric cylinders is considered. Figure 10 shows the scenario, in which the cylinders are identical but with a different rotation angle. Their permittivities are $\epsilon_{r,i} = 3 + 0.05j$, semimajor axis $a = \lambda_0$, and semiminor axis $b = 2\lambda_0$. They are numbered from the left to the right going from bottom to top (see Fig. 10). Their rotation angles are spaced equally as $\{-180, -162, -144, \ldots, 144, 162, 180\}$ degrees, and the center coordinates are equal to $\{(-6, -2), (-4, -2), (-2, -2), \ldots, (2, 2), (4, 2), (6, 2)\}\lambda_0$. The sampling step per wavelength λ_0 is 20, and the incident wave is assumed to be plane $\psi_{\text{inc}}(\boldsymbol{r}) = e^{j\boldsymbol{k}_{\text{inc}}\cdot\boldsymbol{r}} = e^{jk_0(x\sin\theta_{\text{inc}} - z\cos\theta_{\text{inc}})}$, with an incidence angle $\theta_{\text{inc}} = 0$.

Figure 11 plots the RCS in dBm scale versus the scattering angle θ_{sca} (scenario depicted in Fig. 10). The polarization is TM. In the legend, the labels mean "CBFM($\epsilon_{\text{CBFM,SVD}}$-$n_{\text{IPW}}$)-Method: $\bar{N}_{\text{IPW}} - \bar{N}_{\text{IPW,SVD}}$, RRE" (Table 1), where the relative residual error (RRE) is defined by Eq. (42), in which $\boldsymbol{X}$ is the scattered field in far field versus θ_{sca}. "Method" is the method

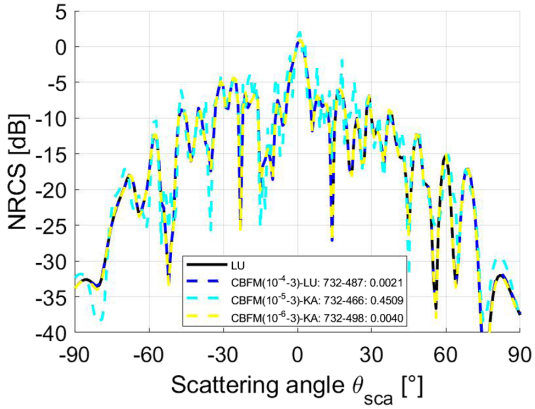

Fig. 9. Same variations as in Fig. 7, but the polarization is TE.

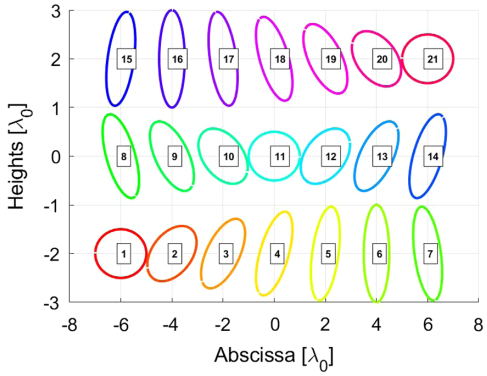

Fig. 10. Scenario 2: Collection of $P = 21$ elliptical dielectric cylinders.

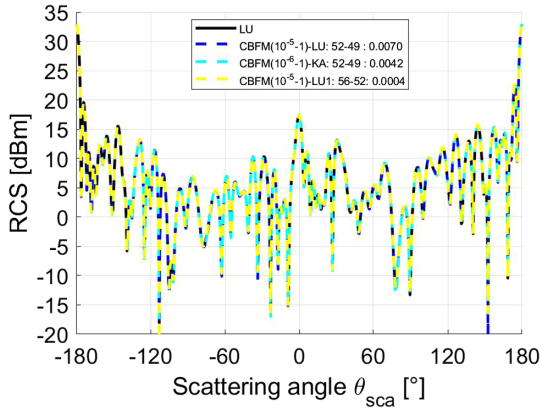

Fig. 11. RCS in dBm scale versus the scattering angle θ_{sca} (scenario depicted in Fig. 10). The polarization is TM.

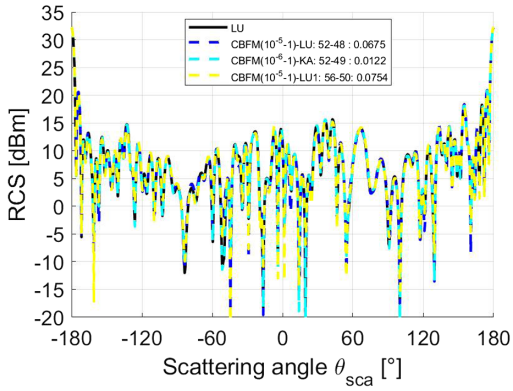

Fig. 12. Same variation as in Fig. 11, but the polarization is TE.

(LU or KA) applied to compute the PBFs. Figure 11 shows that CBFM matches well with LU; further, in comparison with a rough surface, the threshold $\epsilon_{\mathrm{CBFM,SVD}}$ must be lower (divided by 10). The label LU1 means that the self-impedance submatrices $\{\bar{\boldsymbol{Z}}_{i,i}\}$ and their associated PBFs are calculated only for the scatterer 1, since these functions are invariant by rotation and translation (the elliptical cylinders are identical). This property significantly accelerates the first stage of CBFM since the matrices $\{\bar{\boldsymbol{Z}}_{i,i}\}$ and their associated PBFs of the scatterers $i \in [2;\ P]$ are not performed.

In Fig. 11, $n_{\mathrm{IPW}} = 1$, and the legend (see also Table 2) indicates that $\bar{N}_{\mathrm{IPW}}$ does not significantly change in comparison with $\bar{N}_{\mathrm{IPW,SVD}}$. This means that the value $\bar{N}_{\mathrm{IPW}}$ calculated from Eq. (41) is well chosen and that the SVD truncation could be omitted.

Figure 12 plots the same variation as in Fig. 11, but the polarization is TE. The results of the different methods match well with those of LU. The number of unknowns and the size of the reduced matrix for CBFM-LU are reported in Table 2.

For a collection of elliptical cylinders, this second study showed again that the CBFM is efficient and that the value of N_{IPW} expressed by Eq. (41) is well suited. In addition, like for a rough interface (comparison of Fig. 7 with Fig. 9), the TE polarization needs a smaller threshold $\epsilon_{\mathrm{CBFM,SVD}}$ than for the TM one to reach a similar RRE.

C. Scenario 3: Collection of Elliptical Coated Cylinders

In this subsection, the scattering from six elliptical coated dielectric cylinders is considered. Figure 13 shows the scenario. A coated cylinder is composed of three nested cylinders separating four homogeneous media. The scatterers numbered 1, 2, and 3 have semimajor axis $a = \{4, 3, 2\}\lambda_0$, semiminor axis $b = \{3, 2, 1\}\lambda_0$, rotation angles $\{0, 30, 60\}$ degrees, and equal centers of coordinates $(-4.5, 7)\lambda_0$. The permittivities of the four media $\{\Omega_i\}$ $(i \in (1;\ 4))$ are $\epsilon_r = \{1,\ 2 + 0.05j,\ 2.5 + 0.06j,\ 3 + 0.07j\}$. The scatterers $\{7, 8, 9\}$ and $\{13, 14, 15\}$ are obtained from scatterers $\{1, 2, 3\}$ by making a vertical translation of $-7\lambda_0$ and $-14\lambda_0$, respectively. The remaining scatterers defined for $x > 0$ are obtained from those defined for $x < 0$ by symmetry. The sampling step per wavelength λ_0 is 20, and the incident wave is assumed to be plane $\psi_{\mathrm{inc}}(\boldsymbol{r}) = e^{j\boldsymbol{k}_{\mathrm{inc}}\cdot\boldsymbol{r}} = e^{jk_0(x\sin\theta_{\mathrm{inc}} - z\cos\theta_{\mathrm{inc}})}$, with an incidence angle $\theta_{\mathrm{inc}} = 0$.

Figure 14 plots the RCS in dBm scale versus the scattering angle θ_{sca} (scenario depicted in Fig. 13). The polarization is TM. As we can see, a good agreement is obtained between LU and CBFM-LU and CBFM-KA. Like previously, for KA, the threshold $\epsilon_{\mathrm{CBFM,SVD}} = 10^{-6}$ is divided by 100 in comparison with that of LU to select enough PBFs. In Fig. 14, the legend (see also Table 2) indicates that $\bar{N}_{\mathrm{IPW}}$ moderately changes in comparison with $\bar{N}_{\mathrm{IPW,SVD}}$. This means that the value $\bar{N}_{\mathrm{IPW}}$

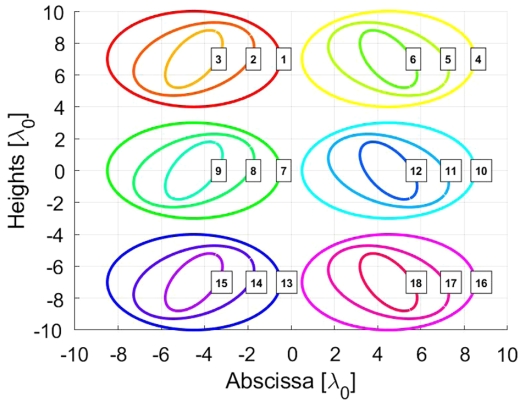

Fig. 13. Scenario 3: Six elliptical dielectric coated cylinders ($P = 18$ scatterers).

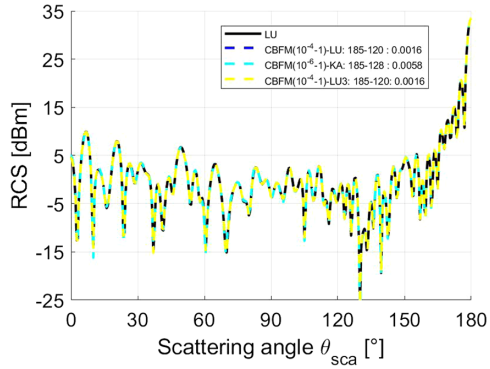

Fig. 14. RCS in dBm scale versus the scattering angle θ_{sca} (scenario depicted in Fig. 13). The polarization is TM.

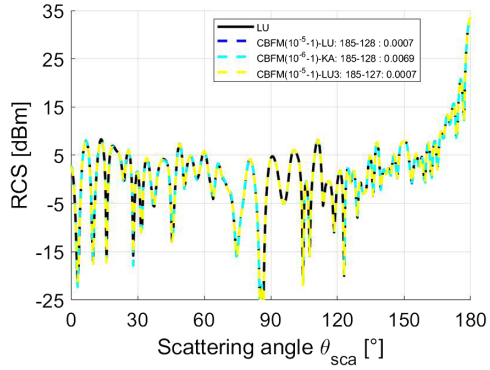

Fig. 15. Same variation as in Fig. 14, but the polarization is TE.

calculated from Eq. (41) is slightly overestimated and that the SVD truncation allows us to decrease the size of the reduced matrix. In the legend, "CBFM-LU3" means that the PBFs and the self-impedance submatrices $\{\bar{\boldsymbol{Z}}_{i,i}\}$ are only computed for the scatterers $i = \{1, 2, 3\}$ (first coated cylinder); the other coated cylinders are identical by translation and rotation (same as the second scenario).

Figure 15 plots the same variation as in Fig. 14, but the polarization is TE. In addition, for CBFM-LU, $\epsilon_{\text{CBFM,SVD}} = 10^{-5}$ is divided by 10 in comparison with the TM polarization. The results perfectly match with those obtained from LU.

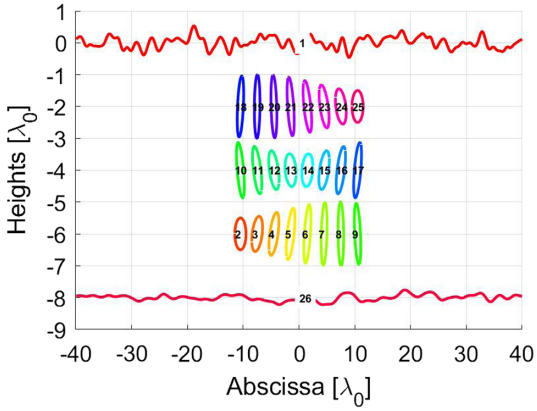

Fig. 16. Scenario 4: Inhomogeneous rough layer composed of two rough interfaces separated by a collection of 24 elliptical cylinders ($P = 26$).

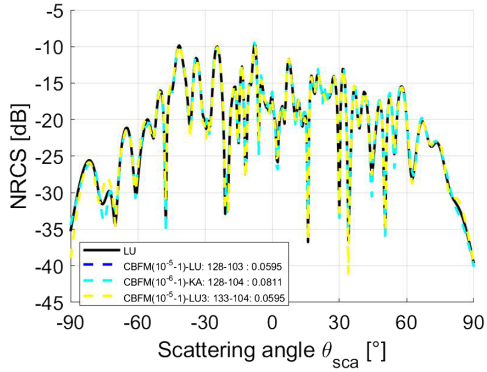

Fig. 17. NRCS in dB scale versus the scattering angle θ_{sca} (scenario depicted in Fig. 16). The polarization is TM.

D. Scenario 4: Inhomogeneous Rough Layer

In this subsection, the field scattered by an inhomogeneous rough layer composed of two rough interfaces separated by a collection of 24 elliptical cylinders is presented ($P = 26$ scatterers).

As shown in Fig. 16, scatterers 1 and 26 are two independent rough interfaces of length $80\lambda_0$ with standard deviations $\sigma_z = \{0.2, 0.1\}\lambda_0$, height correlation lengths $L_c = \{1, 1.5\}\lambda_0$, Gaussian ACFs, and a Gaussian height distribution. They separate three homogeneous media of permittivities $\epsilon_r = \{2 + 0.01j, 3 + 0.02j, 4 + 0.05j\}$. The 24 cylinders are identical but with different rotation angles. Their permittivities are $\epsilon_{r,i} = 4 + 0.05j$ and have a semimajor axis $a = \lambda_0$ and a semiminor axis $b = 0.5\lambda_0$. They are numbered from left to right going from bottom to top (see Fig. 16). Their rotation angles are spaced equally and range from -180 to 180 with a step of 15.65 deg. The sampling step per wavelength λ_0 is 20. As in scenario 1, to attenuate the edge diffraction by the upper surface, Thorsos's [51] tapered incident wave is applied, with $g = L_1/6$, and the incident angle is $\theta_{\text{inc}} = 0$.

Figure 17 plots the NRCS in dB scale versus the scattering angle θ_{sca} (scenario depicted in Fig. 16). The polarization is TM. Figure 18 plots the same variation as in Fig. 17, but the polarization is TE. From Eq. (41), to calculate $N_{\text{IPW},i}$, $n_{\text{IPW}} = 1$

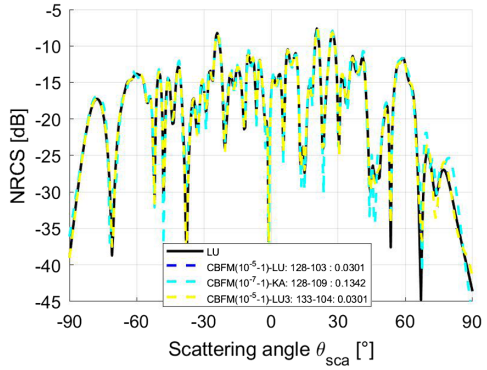

Fig. 18. Same variation as in Fig. 17, but the polarization is TE.

for the cylinders and $n_{\mathrm{IPW}} = 3$, for both rough surfaces. As we can see, a good agreement is obtained between LU and CBFM combined with either LU or KA.

6. CONCLUSION

In this paper, the MoM is generalized to several 2D scatterers of any shape; further, the CBFM combined with LU and KA is addressed for efficiently solving the resulting linear system. Considering four different complex scenarios depicted in Figs. 5, 10, 13 and 16, for both the TM and TE polarizations, the numerical results showed that CBFM-LU and CBFM-KA are efficient in terms of computing time and memory requirements in comparison with the brute force MoM (LU decomposition of the entire matrix of the problem). Table 2 summarizes the performances of CBFM-LU. For a large number of unknowns, N, the efficiency is even better since only the self-impedance submatrices are stored for CBFM and the complexity of LU is $\mathcal{O}(N^3)$.

The calculation of the number of PBFs, $N_{\mathrm{IPW},i}$ given by Eq. (41), is well suited. For a rough surface, $n_{\mathrm{IPW}} = 3$ and for an elliptical cylinder, $n_{\mathrm{IPW}} = 1$. To reduce the size of the reduced matrix, a SVD truncation can be applied; for elliptical cylinders, however, it is not useful because $N_{\mathrm{IPW},i,\mathrm{SVD}}$ is of the same order of $N_{\mathrm{IPW},i}$. For a collection of objects invariant by translation and rotation, another advantage of CBFM is that the PBFs and the self-impedance submatrices of the scatterers are equal. Therefore, the first stage of CBFM is applied only on a single scatterer.

To accelerate the computation of the PBFs, that is, to avoid an LU decomposition on the self-impedance submatrices, KA is applied. The numerical results showed that CBFM-KA matches well with LU, but in comparison with CBFM-LU, the threshold $\epsilon_{\mathrm{CBFM,SVD}}$ must be divided by 100 to obtain a comparable value of $N_{\mathrm{IPW},i}$. It is important to point out that CBFM-KA predicts good results, even on geometries for which KA is not valid, like the elliptical cylinders. In addition, in Eq. (38), the boolean illumination function $\mathcal{I}(\boldsymbol{r})$ can be omitted. This statement is surprising and allows us to simplify the calculation of PBFs. Table 2 shows that the time difference between CBFM-LU and CBFM-KA is small and increases as the number of unknowns grows. As expected, the time is smaller for CBFM-KA. For CBFM-LU, the PBFs are calculated from a LU inversion of complexity $\mathcal{O}(N_i^3)$, whereas for CBFM-KA, the complexity is $\mathcal{O}(N_i)$. Thus, for large N_i (3D problem), CBFM-KA should be competitive. In addition, with CBFM, the allocation time to calculate the reduced characteristic matrix (second stage common to CBFM-LU and CBFM-KA) is about 80%–90% of the total time. In Table 2, this explains the small differences between $t_{\mathrm{CBFM,LU}}$ and $t_{\mathrm{CBFM,KA}}$.

The advantage of the domain decomposition method is that it is highly parallelizable, which further reduces the computing time. The proposed method is then a powerful electromagnetic computation tool to solve any 2D problem, especially when some scatterers are identical.

APPENDIX A: ELEMENTS OF THE MATRICES

In Eq. (1), the elements (m, n) (indexes of the row and column, respectively) of the submatrices $\{\bar{\boldsymbol{A}}_{11}, \bar{\boldsymbol{B}}_{11}, \bar{\boldsymbol{C}}_{11}, \bar{\boldsymbol{D}}_{11}\}$ are expressed as $(p = q = 1)$

$$A_{pq,mn} = \begin{cases} -\frac{jk_0 v_{q,n}|\Delta_{q,n}|}{4} \frac{\mathrm{H}_1^{(1)}(k_0\|\boldsymbol{r}_{q,n}-\boldsymbol{r}_{p,m}\|)}{\|\boldsymbol{r}_{q,n}-\boldsymbol{r}_{p,m}\|} \left[\gamma_{q,n}(x_{q,n}-x_{p,m}) - (z_{q,n}-z_{p,m})\right] & \text{for } m \neq n \\ +\frac{1}{2} - \frac{v_{q,n}|\Delta_{q,n}|}{4\pi} \frac{\gamma'_{q,n}}{1+\gamma_{q,n}^2} & \text{for } m = n \end{cases}, \tag{A1}$$

$$B_{pq,mn} = \frac{j|\Delta_{q,n}|\sqrt{1+\gamma_{q,n}^2}}{4} \begin{cases} \mathrm{H}_0^{(1)}(k_0\|\boldsymbol{r}_{q,n}-\boldsymbol{r}_{p,m}\|) & \text{for } m \neq n \\ \left[1 + \frac{2j}{\pi}\ln\left(0.164k_0\sqrt{1+\gamma_{q,n}^2}|\Delta_{q,n}|\right)\right] & \text{for } m = n \end{cases}, \tag{A2}$$

$$C_{pq,mn} = \begin{cases} A_{pq,mn}\big|_{k_0=k_1} & \text{for } m \neq n \\ -\frac{1}{2} - \frac{v_{q,n}|\Delta_n|}{4\pi} \frac{\gamma'_{q,n}}{1+\gamma_{q,n}^2} & \text{for } m = n \end{cases}, \tag{A3}$$

$$D_{pq,mn} = \frac{B_{pq,mn}\big|_{k_0=k_1}}{\rho_{01}}. \tag{A4}$$

where $\boldsymbol{r}_{q,n} = (x_{q,n}, z_{q,n}) \in S_q$ (coordinates of the point on the surface S_q), $\boldsymbol{r}_{p,m} = (x_{p,m}, z_{p,m}) \in S_p$, $\gamma = dz/dx$, $\gamma' = d\gamma/dx$, $\Delta_{q,n}$ the sampling step on S_q, $v_{q,n} = \mathrm{sgn}(\hat{\boldsymbol{n}}_{q,n} \cdot \hat{\boldsymbol{z}})$ ($\hat{\boldsymbol{n}}_{q,n}$ is the unitary vector normal to the surface S_q at the point $\boldsymbol{r}_{q,n}$), $\mathrm{H}_0^{(1)}$ the zeroth order Hankel function of the first kind and $\mathrm{H}_1^{(1)}$ its derivative.

For the TE polarization, the variable $\rho_{01} = 1$, whereas for the TM polarization, $\rho_{01} = \epsilon_{r,0}/\epsilon_{r,1}$, where $\epsilon_{r,i}$ is the relative permittivity of medium Ω_i.

It is important to underline that, for a self (interaction of the same surface) impedance submatrix, $p = q$ and a singularity occurs for $m = n$, whereas for a coupling matrix $p \neq q$, there is no singularity because $\boldsymbol{r}_p \neq \boldsymbol{r}_q$. In addition, any matrix $\bar{\boldsymbol{Z}}_{pq}$ propagates the field from the source points $\{\boldsymbol{r}_{q,n}\}$ toward the observation points $\{\boldsymbol{r}_{p,m}\}$.

For the calculation of the scattered field in the far field ($u \to \infty$), the following expansions [6] of the Hankel functions can be applied:

$$\begin{cases} H_0^{(1)}(u) \approx \sqrt{\frac{2}{\pi u}} \exp\left[j\left(u - \frac{\pi}{4}\right)\right] \\ H_1^{(1)}(u) = -jH_0^{(1)}(u) \end{cases}. \quad \textbf{(A5)}$$

Disclosures. The authors declare no conflicts of interest.

Data Availability. Data underlying the results presented in this paper are not publicly available at this time but may be obtained from the authors upon reasonable request.

REFERENCES

1. F. Frezza, F. Mangini, and N. Tedeschi, "Introduction to electromagnetic scattering: tutorial," J. Opt. Soc. Am. A **35**, 163–173 (2018).
2. F. Frezza, F. Mangini, and N. Tedeschi, "Introduction to electromagnetic scattering, part ii: tutorial," J. Opt. Soc. Am. A **37**, 1300–1315 (2021).
3. G. D. Tsogkas, J. A. Roumeliotis, and S. P. Savaidis, "Electromagnetic scattering by an infinite elliptic dielectric cylinder with small eccentricity using perturbative analysis," IEEE Trans. Antennas Propag. **58**, 107–205 (2010).
4. G. P. Zouros, "Electromagnetic plane wave scattering by arbitrarily oriented elliptical dielectric cylinders," J. Opt. Soc. Am. A **28**, 2376–2384 (2011).
5. G. P. Zouros, "Oblique electromagnetic scattering from lossless or lossy composite elliptical dielectric cylinders," J. Opt. Soc. Am. A **30**, 196–205 (2013).
6. M. Abramowitz and I. A. Stegun, *Handbook of Mathematical Functions* (Dover, 1970).
7. A. Sommerfeld, *Lectures on Theoretical Physics* (Academic, 1964), Vol. **6**.
8. H. A. Youssif and S. Kohler, "Scattering by two penetrable cylinders at oblique incidence. I. The analytical solution," J. Opt. Soc. Am. A **5**, 1085–1096 (1988).
9. P. J. Valle, F. Gonzalez, and F. Moreno, "Electromagnetic wave scattering from conducting cylindrical structures on flat substrates: study by means of the extinction theorem," Appl. Opt. **33**, 512–523 (1994).
10. A. Madrazo and M. Nieto-Vesperinas, "Scattering of electromagnetic waves from a cylinder in front of a conducting plane," J. Opt. Soc. Am. A **12**, 1298–1309 (1995).
11. G. Videen and D. Ngo, "Light scattering from a cylinder near a plane interface: theory and comparison with experimental data," J. Opt. Soc. Am. A **14**, 70–78 (1997).
12. B. H. Henin, A. Z. Elsherbeni, and M. H. A. Sharkawy, "Oblique incidence plane wave scattering from an array of circular dielectric cylinders," Prog. Electromagn. Res. **68**, 261–279 (2007).
13. S. Ahmed and Q. A. Naqvi, "Electromagnetic scattering from a perfect electromagnetic conductor cylinder buried in a dielectric half-space," Prog. Electromagn. Res. **78**, 25–38 (2008).
14. S.-C. Lee, "Scattering by closely spaced parallel non homogeneous cylinders in an absorbing medium," J. Opt. Soc. Am. A **28**, 1812–1819 (2011).
15. P. Pawliuk and M. Yedlin, "Scattering from cylinders using the two-dimensional vector plane wave spectrum," J. Opt. Soc. Am. A **28**, 1177–1184 (2011).
16. P. Pawliuk and M. Yedlin, "Scattering from cylinders near a dielectric half-space using a general method of images," J. Opt. Soc. Am. A **66**, 5296–5304 (2012).
17. A. F. Fiaz, F. Frezza, L. Pajewski, C. Ponti, and G. Schettini, "Scattering by a circular cylinder buried under a slightly rough surface: the cylindrical-wave approach," IEEE Trans. Antennas Propag. **60**, 2834–2842 (2012).
18. C. Amra, "Light scattering from multilayer optics. I. Tools of investigation," J. Opt. Soc. Am. A **11**, 197–210 (1994).
19. I. Ohlidal and K. Navratil, "Scattering of light from multilayer systems with rough boundaries," Prog. Opt. **34**, 251–334 (1995).
20. I. M. Fuks and A. G. Voronovich, "Wave diffraction by rough interfaces in an arbitrary plane-layered medium," Waves Random Media **10**, 253–272 (2000).
21. A. Soubret, G. Berginc, and C. Bourrely, "Backscattering enhancement of an electromagnetic wave scattered by two dimensional," J. Opt. Soc. Am. A **18**, 2778–2788 (2001).
22. A. Tabatabaeenejad and M. Moghaddam, "Bistatic scattering from dielectric structures with two rough boundaries using the small perturbation method," IEEE Trans. Geosci. Remote Sens. **44**, 2102–2114 (2006).
23. M. Sanamzadeh, L. Tsang, J. T. Johnson, R. J. Burkholder, and S. Tan, "Scattering of electromagnetic waves from 3D multilayer random rough surfaces based on the second-order small perturbation method: energy conservation, reflectivity, and emissivity," J. Opt. Soc. Am. A **34**, 395–409 (2017).
24. R. Dusséaux and A. Saddek, "Level crossing rate and average fade distance of signal scattering from rough layered interfaces," IEEE Trans. Antennas Propag. **66**, 1999–2007 (2018).
25. N. Pinel, C. Bourlier, and J. Saillard, "Bistatic scattering from one-dimensional random rough homogeneous layers in the high-frequency limit with shadowing effect," Waves Random Complex Media **17**, 283–303 (2007).
26. N. Pinel and C. Bourlier, "Scattering from very rough layers under the geometric optics approximation: further investigation," J. Opt. Soc. Am. A **25**, 1293–1306 (2008).
27. N. Pinel, J. T. Jonhson, and C. Bourlier, "A geometrical optics model of three dimensional scattering from a rough surface over a planar surface," IEEE Trans. Antennas Propag. **57**, 546–554 (2009).
28. R. F. Harrington, *Field Computation by Moment Method* (Macmillan, 1968).
29. L. Tsang, J. A. Kong, K.-H. Ding, and C. O. Ao, *Scattering of Electromagnetic Waves, Numerical Simulations* (Wiley, 2000).
30. C. Bourlier, N. Pinel, and G. Kubické, *Method of Moments for 2D Scattering Problems. Basic Concepts and Applications*, Focus series (ISTE Ltd/Wiley, 2013).
31. Q. Sun, E. Klaseboer, A. J. Yuffa, and D. Y. C. Chan, "Field-only surface integral equations: scattering from a perfect electric conductor," J. Opt. Soc. Am. A **37**, 276–283 (2020).
32. J. T. Johnson and R. J. Burkholder, "Coupled canonical grid/discrete dipole approach for computing scattering from objects above or below a rough interface," IEEE Trans. Geosci. Remote Sens. **39**, 1214–1220 (2001).
33. J. T. Johnson, "A numerical study of scattering from an object above a rough surface," IEEE Trans. Antennas Propag. **50**, 1361–1367 (2002).
34. H. Ye and Y. Q. Jin, "Fast iterative approach to difference electromagnetic scattering from the target above a rough surface," IEEE Trans. Geosci. Remote Sens. **44**, 108–115 (2006).
35. H. Ye and Y. Q. Jin, "A hybrid analytic-numerical algorithm of scattering from an object above a rough surface," IEEE Trans. Antennas Propag. **45**, 1174–1180 (2007).
36. C. Dong, C. Wang, X. Wei, and H. H. Yin, "EM scattering from complex targets above a slightly rough surface," Prog. Electromagn. Res. **3**, 685–688 (2007).
37. N. Déchamps and C. Bourlier, "Electromagnetic scattering from a rough layer: propagation-inside-layer expansion method combined to an updated BMIA/CAG approach," IEEE Trans. Antennas Propag. **55**, 2790–2802 (2007).
38. N. Déchamps and C. Bourlier, "Electromagnetic scattering from a rough layer: propagation-inside-layer expansion method combined to the forward-backward novel spectral acceleration," IEEE Trans. Antennas Propag. **55**, 3576–3586 (2007).
39. G. Kubické, C. Bourlier, and J. Saillard, "Scattering by an object above a randomly rough surface from a fast numerical method: extended PILE method combined to FB-SA," Waves Random Complex Media **18**, 495–519 (2008).
40. J. Laviada, M. R. Pino, and F. Las-Heras, "Generation of excitation-independent characteristic basis functions for three-dimensional momogeneous dielectric bodies," IEEE Trans. Antennas Propag. **59**, 3318–3327 (2011).
41. C. Bourlier, N. Pinel, and G. Kubické, "Propagation-inside-layer-expansion method combined with physical optics for scattering by

coated cylinders, a rough layer, and an object below a rough surface," J. Opt. Soc. Am. A **30**, 1727–1737 (2013).
42. C. Bourlier, C. Le Bastard, and V. Baltazard, "Generalization of PILE method to the EM scattering from stratified subsurface with rough interlayers: application to the detection of debondings within pavement structure," IEEE Trans. Geosci. Remote Sens. **53**, 4104–4115 (2015).
43. C. Li and R. Mittra, "Characteristic basis function method for fast analysis of 3-D scattering from objects buried under rough surfaces," IEEE Trans. Geosci. Remote Sens. **57**, 5252–5265 (2019).
44. V. S. Prakash and R. Mitra, "Characteristic basis function method: a new technique for efficient solution of method of moments matrix equations," Microw. Opt. Technol. Lett. **36**, 95–100 (2003).
45. C. Bourlier, Y. Arencibia Noa, and G. Kubické, "Two domain decomposition methods, SDIM and CBFM, for the scattering from a two-dimensional perfectly-conducting rough surface: comparison and parametric study," J. Opt. Soc. Am. A **37**, 1512–1525 (2020).
46. N. Déchamps, N. De Beaucoudrey, C. Bourlier, and S. Toutain, "Fast numerical method for electromagnetic scattering by rough layered interfaces: propagation-inside-layer expansion method," J. Opt. Soc. Am. A **23**, 359–369 (2006).
47. C. Bourlier, S. Bellez, and G. Kubické, "Sub-domain decomposition iterative method combined with ACA: an efficient technique for the scattering from a large highly conducting rough sea surface," IEEE Trans. Antennas Propag. **63**, 659–666 (2015).
48. E. Lucente, A. Monorchio, and R. Mittra, "An iteration-free MoM approach based on excitation independent characteristic basis functions for solving large multiscale electromagnetic scattering problems," IEEE Trans. Antennas Propag. **56**, 999–1007 (2008).
49. L. M. Brekhovskikh, *Waves in Layered Media*, 2nd ed. (Academic, 1980).
50. C. Bourlier, *Radar Propagation and Scattering in a Complex Maritime Environment* (ISTE/Elsevier, 2018).
51. E. I. Thorsos, "The validity of the Kirchhoff approximation for rough surface scattering using a Gaussian roughness spectrum," J. Acoust. Soc. Am. **83**, 78–92 (1988).
52. F. T. Ulaby, R. K. Moore, and A. K. Fung, *Microwave Remote Sensing: Active and Passive* (1982), Vol. **2**.
53. R. J. Papa and J. F. Lennon, "Conditions for the validity of physical optics in rough surface scattering," IEEE Trans. Antennas Propag. **36**, 647–650 (1988).